Self consistent one-dimensional hybrid code simulations of a relaxing field reversal

Alan Richardson[1] and Sandra C. Chapman

Space Science Centre (MAPS), University of Sussex, Brighton, United Kingdom

Abstract. We present the results of self-consistent one-dimensional hybrid code (kinetic ions and fluid electrons) simulations of a dipolarizing field reversal. Local ion energization processes are studied in terms of both the ion kinetics and bulk plasma behavior. We demonstrate evolution of the system through two phases: (1) a quasi-static "trapping" phase, during which inflowing ions are trapped in the reversal structure at early times and (2) a dynamic "escape" phase, during which trapped ions escape from the reversal after an increase in $P_{\parallel}$. We perform simulations with different linking field component (GSE B_z) to reversing component (GSE B_x) ratios and show that this parameter controls the details of the ion energization. This study suggests a characteristic signature in the magnetic field (a bipolar B_y) and bulk plasma parameters (an increase in $P_{\parallel}$) associated with this behavior which should be observable in in situ data. Our results are applicable for times earlier than the midtail to ionosphere Alfvén travel time.

1. Introduction

At the onset of a magnetic substorm, magnetic field lines in the near-Earth geotail undergo rapid reconfiguration from a taillike geometry to a more dipolar state ("dipolarization"). Characteristic features of dipolarization include rapid changes in the local field strength, the observation of high-energy ($\sim 1 MeV$) bursts of particles [e.g., *Hones et al.*, 1976], and the arrival of lower-energy plasma seen at around $6R_E$ (so called "injection events") [e.g., *Lennartson et al.*, 1981]. To date, only non-self-consistent studies have been made of ion dynamics during dipolarization [e.g., *Chapman*, 1993, 1994; *Delcourt*, 1991; *Delcourt and Moore*, 1992].

In this paper we present one-dimensional hybrid code simulations of a dipolarizing field reversal. In order to study the consequences of dynamic reconfiguration of the magnetotail magnetic field at substorm onset we choose as our initial condition an out-of-equilibrium field reversal. This work is significant in that unlike previous studies of ion energization during dipolarization [e.g., *Delcourt*, 1991; *Delcourt and Moore*, 1992], we can self-consistently examine the evolution of local field structure and ion dynamics. The ion energization mechanisms which occur are all local to the dipolarizing field line, enabling us to deduce what energization can occur locally and by implication what must occur elsewhere (e.g., at a reconnection site).

We present the results of two simulations, one with a weak linking field component and one with a stronger linking field. The values we use span the range of observed linking field component. We demonstrate that the ratio of linking field to reversing field components determines the details of ion energization, rather than the overall evolution of the relaxing reversal.

We find that the reversing magnetic field structure is capable of trapping inflowing ions. As the trapped ions oscillate across the reversal, they gain net field-aligned acceleration via a mechanism approximately modelled as first-order Fermi acceleration. The parallel pressure of the trapped population increases due to individual ion acceleration, and once it has become sufficiently large to strongly perturb the bulk plasma configuration, the trapped population escapes. The escaping population may be in pressure balance or may have an overpressure, depending on the size of the linking field. After the escape of the initially trapped population, a continual process evolves in which ions initially located outside of the reversal convect in, are trapped, accelerate, and escape *en masse*. A characteristic bipolar B_y field component evolves across the reversal.

The paper will be structured as follows. We first give an overview of the simulation, provide details of the simulation method, and describe the initial conditions in more depth. We then present and discuss the results of two typical simulations. Finally, we summarize our key results.

---

[1]Now at Tessella Support Services, Abingdon, United Kingdom.

2. Simulation Details

2.1. Overview

An overview of the simulation geometry is given in Figures 1a (initial configuration) and 1b (subsequent evolution). The one-dimensional hybrid code employed here allows variation in one direction only (GSE z) but retains all three vector components. The field reversal is initially out of equilibrium, in that the $\mathbf{J} \times \mathbf{B}$ force is not balanced by the initially isotropic ion distribution. The field lines therefore relax as time increases, accelerating the plasma. The system is therefore analogous to the evolution of a reversal when the associated plasma population has (by some unstated mechanism) been newly isotropized. The relaxation of the reversal in the simulation occurs by some combination of fast, slow, and Alfvén waves which can propagate in GSE $\pm z$ as the field lines in principle contract in GSE$+x$ as shown in Figure 1b. This generates a strong field region with inflowing isotropic plasma outside of the reversal, and a weak field region in the reversal within which plasma is accelerated, and within which also particles can become trapped.

2.2. Simulation Model

The simulations are performed using a one- dimensional hybrid code, in which the electron population constitutes a massless, charge-neutralizing fluid background and the ions (protons) are represented by computational particles. The simulation grid size and time step are such that the ion gyromotion is fully resolved. In this limit the full range of "low-frequency" (i.e., $\omega \ll \omega_{pe}, \omega_{ce}$) phenomena are resolved. Quantities vary in one direction only, which we orient in $\hat{z}$ GSE; however all three vector components are retained.

The governing equations are

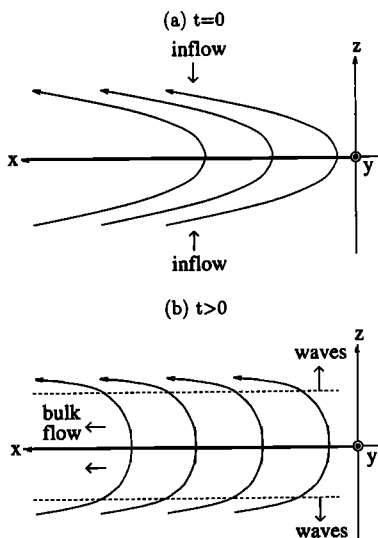$$\frac{\partial n}{\partial t} + \nabla \cdot [n\mathbf{V}] = 0 \qquad (1)$$

(a) t=0

inflow

(b) t>0

waves

bulk flow

waves

Figure 1. The magnetic field configuration envisaged (a) at time zero and (b) at some later time.

$$\frac{d\mathbf{v}_i^{\#}}{dt} = e(\mathbf{E} + \mathbf{v}_i^{\#} \times \mathbf{B}) \qquad (2)$$

$$\nabla \times \mathbf{E} = -\frac{\partial \mathbf{B}}{\partial t} \qquad (3)$$

$$\nabla \times \mathbf{B} = \mu_0 \mathbf{J} \qquad (4)$$

$$\nabla \cdot \mathbf{J} = 0 \qquad (5)$$

$$\mathbf{E} = -\mathbf{V}_i \times \mathbf{B} + \frac{\mathbf{J} \times \mathbf{B}}{ne} - \frac{\nabla P_e}{ne} + \eta \mathbf{J} \qquad (6)$$

where the electron inertial term has been neglected, and quasineutrality implies $n\mathbf{V} = n_i \mathbf{V}_i + n_e \mathbf{V}_e$ and $\mathbf{J} = ne(\mathbf{V}_i - \mathbf{V}_e)$. The number density n, and the bulk ion velocity $\mathbf{V}_i$ are obtained directly as moments from the positions and velocities (the $\mathbf{v}_i^{\#}$) of the computational particles that represent the ions. In this one- dimensional geometry the assumption of quasi-neutrality, and continuity of charge, imply that $J_z = 0$ (equation 5), while $\nabla \cdot \mathbf{B} = 0$ constrains B_z to be constant. Full details of the numerical scheme are given by *Terasawa et al.* [1986], with the exception that in order to obtain the electron pressure P_e, Terasawa et al. assume a polytropic equation of state for the electron fluid whereas we obtain P_e from the massless fluid energy equation:

$$\frac{\partial P_e}{\partial t} + \mathbf{V_e} \cdot \nabla P_e = -\gamma P_e \nabla \cdot \mathbf{V_e} + (\gamma - 1)\eta J^2 \qquad (7)$$

where γ is the ratio of specific heats. Equations (1)-(7) form a closed set, with seven unknowns ($\mathbf{E}$, $\mathbf{B}$, n, $\mathbf{V}_i$, $\mathbf{V_e}$, $\mathbf{J}$, and P_e) and seven equations. We selected the code originally developed by *Terasawa et al.* [1986] because it is in principle nonresistive, that is, in the region of the evolving field reversal the resistivity $\eta = 0$ (although, of course, there is numerical resistivity present). This gives the code good resolution, appropriate for studying the fine structure at the edges of the reversal.

Equation (6) can be rewritten using equation (4) for $\mathbf{J}$ and a vector identity to give

$$\mathbf{E} = -\mathbf{V}_i \times \mathbf{B} + \frac{(\mathbf{B} \cdot \nabla)\mathbf{B}}{\mu_0 ne} - \frac{1}{ne}\nabla(\frac{B^2}{2\mu_0} + P_e) + \eta \mathbf{J}. \qquad (8)$$

The five terms in equation (8) represent the forces acting on ions in the simulation. The $\mathbf{V}_i \times \mathbf{B}$ term can play a role in the coupling of different species in a multispecies plasma, where the species differ in mass [*Chapman and Dunlop*, 1986; *Chapman and Schwartz*, 1987] or represent populations of the same particle type with different distribution functions [*Leroy*, 1983]. The $(\mathbf{B} \cdot \nabla)\mathbf{B}$ term represents the curvature force due to the reversing field geometry illustrated in Figure 1a. Since $\mathbf{B} = \mathbf{B}(z,t)$ here, the components of this expression are $B_z \partial/\partial z(\hat{x}B_x + \hat{y}B_y)$. At least initially in the simulation there is no field component in $\hat{y}$, and so this curvature force simply acts to accelerate the plasma in $\hat{x}$ (i.e., the direction in which the field relaxes). Subsequently a B_y component develops and the dynamics become more complex. The third term on the right-hand side of equation (8), involving ∇B^2, is the field pressure term, and this acts toward the center of the field reversal along $\hat{z}$ to initially trap particles in the

reversal. The fact that the curvature and field pressure terms act in different directions shows that the physics of the simulation should not be thought of as being purely one-dimensional; the propagation of waves along $\hat{z}$ allows the reversal to collapse and liberate field energy to the ions as a bulk plasma acceleration in $\hat{x}$ (as illustrated in Figure 1b).

Solution of the above equations requires the specification of suitable boundary conditions: in these simulations we have open "inflow" at both boundaries, so that at the boundaries the bulk plasma parameters and ion distribution functions are held constant. To absorb waves approaching the boundaries, we increase η from zero at the center of the box to a finite value at the edges of the box.

A one-dimensional (i.e. dependence only on z and t) simulation has been chosen for this study to allow good spatial and temporal resolution. This is appropriate as we are examining the local dynamics of an evolving system which does not include coupling with the magnetosphere as a whole, that is, the boundary conditions simply damp waves and absorb particles incident upon them and do not attempt to mimic the ionospheric plasma which in a global model the field lines would ultimately encounter. We therefore do not expect to obtain results of a "global" nature, such as the width of the current sheet in $\hat{y}$ or the implications for the time evolution of current structures in the ionosphere.

Our choice of boundary conditions also implies that we cannot study the evolution of this configuration to equilibrium, since again, this would require coupling between the region of plasma sheet we are numerically modeling and the external system composed of the ionosphere and the Earth's dipolar magnetic field. The coupling would involve appropriate boundary conditions and would require a simulation code allowing spatial variation in more than one dimension (such as the two-dimensional hybrid code used by *Thomas et al.* [1990]). Instead, the study is designed to explore the implications of dynamic changes in the magnetotail field geometry at substorm onset, where by some unstated mechanism the plasma distribution function is isotropized and no longer balances the $\mathbf{J} \times \mathbf{B}$ force of the extended magnetotail field. This phenomenon, "localized" in both space and time, will transfer field energy to the plasma and result in ion energization. The question addressed here is whether this local phenomenon can completely account for the energetic ion signatures seen during ion injection events, or whether energization from some source remote from the simulation region (i.e., remote from the dipolarizing field line) is also required.

Previous studies [*Swift and Allen*, 1987; *Swift*, 1992] have employed two-dimensional particle-in-cell simulations to examine "global" properties of a plasma sheet by using boundary conditions that attempt to mimic the ionosphere. The system modelled was however, essentially in equilibrium and hence did not evolve as an expanding (i.e. dipolarizing) field reversal as expected

here (Figure 1); we shall see that this expanding field reversal drives the overall ion dynamics. In addition, the spatial resolution employed in the above papers would not be sufficient to reveal the detailed structure of the reversal found in this study. The results found here and those in the above papers are therefore complementary, as they are designed to examine different features of plasma sheet behavior.

2.3. Initial Conditions

We represent the predipolarization conditions as an out-of- equilibrium field reversal. The field component B_x is allowed to reverse smoothly at the center of the simulation box, its variation with position z along the simulation axis being given by

$$B_x = B_{x0} \tanh(\frac{z - L/2}{A_0}) \qquad (9)$$

where L is the simulation box length and A_0 is the initial half width of the reversal region. A smaller linking field component parallel to the simulation axis B_z threads the reversal. This component is constrained to be a constant by $\nabla \cdot \mathbf{B} = 0$ in a one dimensional system. The third field component, B_y, is initially zero. These initial conditions describe sharply bent field lines whose only direction of variation is along $\hat{z}$ (Figure 1a). Note that the constant linking field allows us to transform to different E_y convection frames by moving with constant speed in the $\hat{x}$ direction (the de Hoffman Teller transformation [*de Hoffman and Teller*, 1950]).

We find that the parameter which determines the details of ion energization is the ratio of the linking field component B_z to the reversing component B_x. Ion acceleration in x occurs on the scale of the Alfvén speed $V_{A,x}$, whilst the reversal structure expands in z at approximately $V_{A,z}$. Consequently, we present two simulations in which B_{x0} is the same ($20nT$), but B_z is small in the first case ($2nT$) and large in the second ($8nT$). Both these values are consistent with observations [e.g., *Wagner et al.*, 1979]. All other bulk parameters are the same in both simulations.

In the simulation rest frame, plasma flows into the reversal region from both sides with an inflow speed of $0.1V_{A,x}$. The total plasma density is initially constant across the box, at $n_0 = 0.2cm^{-3}$. The plasma has an ion beta of approximately 0.1, whilst the electron temperature is taken to be $\sim 0.1T_i$ [e.g., *Baumjohann et al.*, 1989].

The simulation axis is divided into 512 grid cells. There are approximately 8 grid cells to an ion gyro-orbit, giving good spatial resolution. The time step interval is about 1/400 of the ion gyroperiod. The statistical fluctuation associated with representing the ion population by N_c particles per cell is expected to be $\sim \sqrt{N_c}$. We typically take 100 particles per cell, reducing fluctuations to better than 10%.

2.4. Electrostatic Potential

When discussing the simulation results we make frequent reference to the electric potential ϕ. This is de-

fined in general by

$$\mathbf{E} = -\nabla\phi - \frac{\partial \mathbf{A}}{\partial t} \qquad (10)$$

where $\mathbf{A}$ is the vector potential. The simulation geometry ($\mathbf{B}=\mathbf{B}(z,t)$ and $\mathbf{E}=\mathbf{E}(z,t)$) does not uniquely specify ϕ and $\mathbf{A}$, and here we use for convenience

$$E_x = -\frac{\partial A_x}{\partial t}(z,t) \qquad (11)$$

$$E_y = -\frac{\partial A_y}{\partial t}(z,t) \qquad (12)$$

$$E_z = -\frac{\partial \phi}{\partial z}(z,t) \qquad (13)$$

We find that the general character of the potential ϕ is that of a potential well, due to the effect of the ∇B^2 (field pressure) term in equation (8) discussed earlier. This potential well is capable of trapping inflowing ions.

3. Results

We now present the results of two simulation experiments, which differ only in the ratio of constant linking field component B_z to the reversing field component B_x.

3.1. Overview

We first observe a weak burst of fast magnetohydrodynamic waves from the reversal region. These arise due to the lack of pressure balance inherent in our choice of initial conditions. The fast waves are evident in Figure 2, a snapshot of magnetic field pressure, potential, and magnetic field components taken soon after time zero. Figures 3 and 4 show various plasma parameters plotted against GSE z, the direction of variation in the simulation. Figure 3 is for the weak linking field case, Figure 4 for a strong linking field. In both cases, quantities are given at early and late times in the simulation.
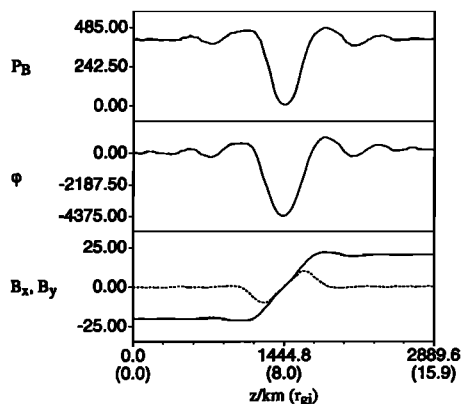
Figure 2. A snapshot of magnetic field pressure P_B ($Nm^{-2} \times 10^{-10}$), potential ϕ (V) and B_x (solid) and B_y (dashed) magnetic field components (nT) taken after 0.6 s ($0.2\tau_{gi}$, where τ_{gi} is the ion gyroperiod) with $B_z = 2nT$. A short train of weak fast magnetohydrodynamic waves is evident.
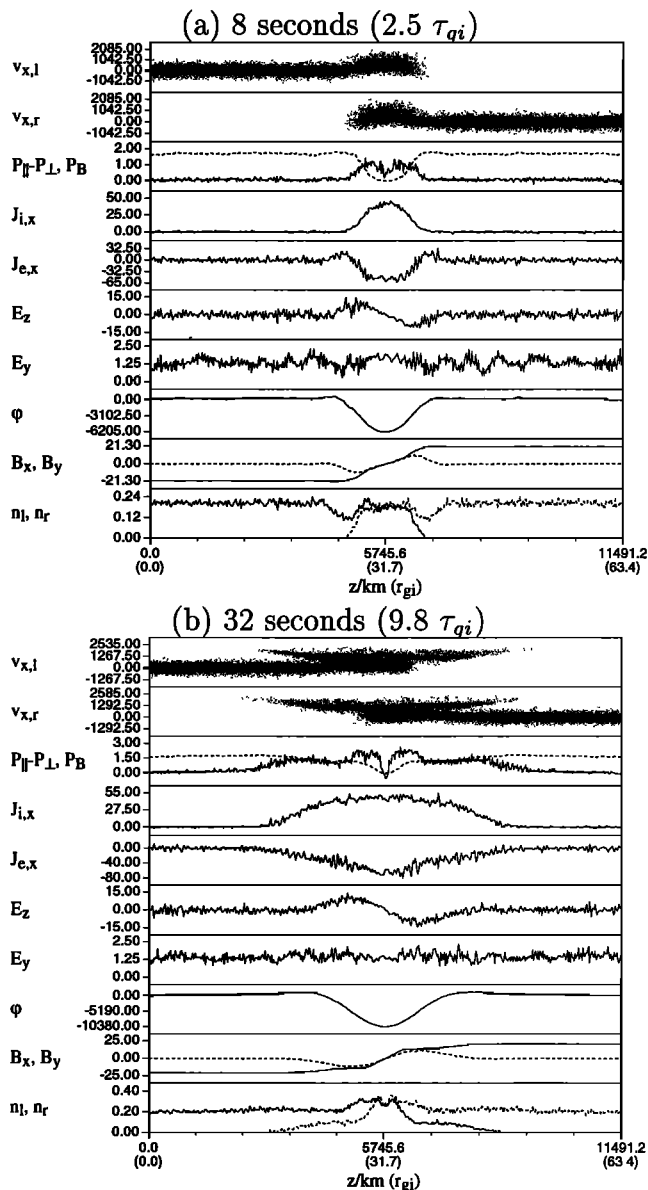
Figure 3. Plasma parameters taken (a) before (b) after the escape of ions trapped in the reversal structure. The linking field is $2nT$. The quantities shown in each figure are as follows. The top two panels show the V_x phase space configuration of the left- and right- hand populations (in kms^{-1}). The next panel shows $P_{\parallel} - P_{\perp}$ (solid) and field pressure P_B (dashed) ($Nm^{-2} \times 10^{-10}$). We then give ion and electron currents in the $\hat{x}$ direction ($A \times 10^{-9}$). The electric field components E_z and E_y ($Vm^{-1} \times 10^{-3}$) and potential ϕ (V) follow. Finally, we give the magnetic field components B_x (solid) and B_y (dashed) (nT), and the density of particles originating from the left- hand (solid) and right- hand (dashed) sides of the box (in cm^{-3}).

Figures 3 and 4 show the potential well associated with the reversing field structure. At early times the well is approximately 20 ion gyroradii across, and it expands in z as the reversal relaxes. The boundaries to the well show a combination of Alfvénic (e.g., constant field pressure) and slow wave (e.g., density depression)
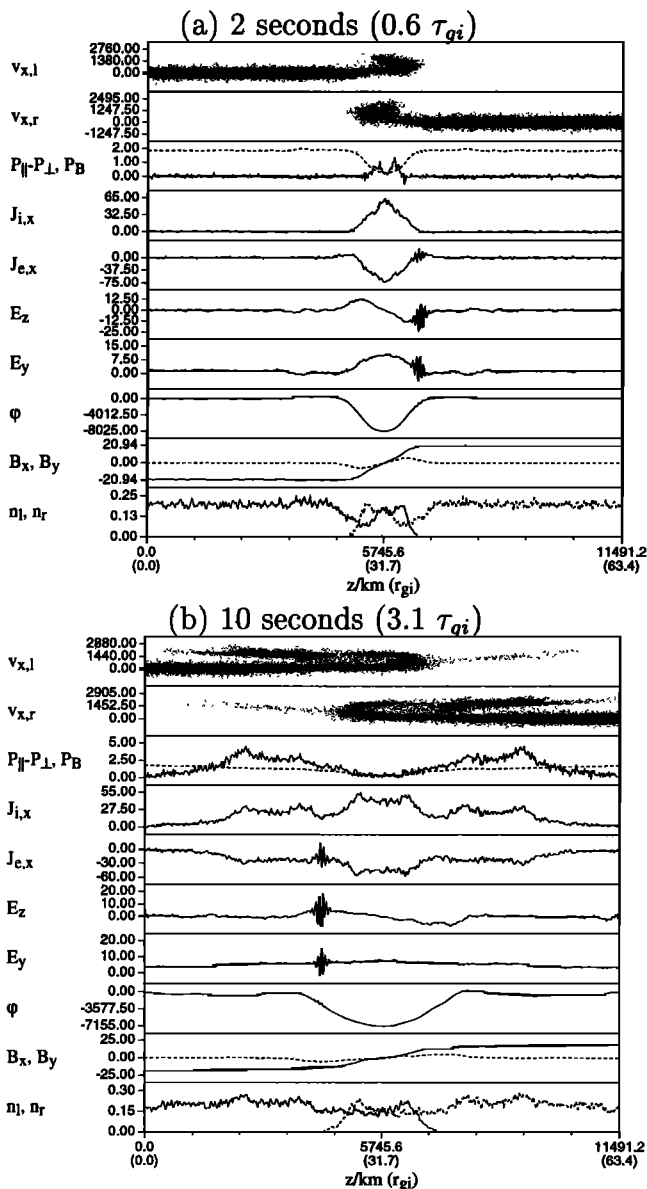
(a) 2 seconds (0.6 τ_{gi})

(b) 10 seconds (3.1 τ_{gi})

Figure 4. As for Figure 3 but with a stronger linking field ($8nT$). Note that escape from the reversal region occurs earlier than with a weaker linking field. It has been verified by examining individual ion trajectories (see e.g., Figure 12) that the noise generated in **E** at the reversal boundaries does not perturb the ion motion.

properties and are approximately 4 ion gyroradii wide. With a linking field $B_z = 2nT$ the boundaries have velocity in $\pm z$ of $\sim 50 km s^{-1}$, compared with slow wave and Alfvén speeds along z of $30 km s^{-1}$ and $98 km s^{-1}$ respectively. With a linking field $B_z = 8nT$ the boundary velocity is $\sim 120 km s^{-1}$, compared with slow wave and Alfvén speeds along z of $110 km s^{-1}$ and $400 km s^{-1}$ A bipolar B_y component develops across the reversal.

A population of trapped ions builds up in the reversal. Some of these ions lay within the weak-field region of the reversal when the simulation began; others were initially located outside and have convected into the weak-field region. Trapped ions accelerate in GSE x as they oscillate across the reversal in z; consequently, the
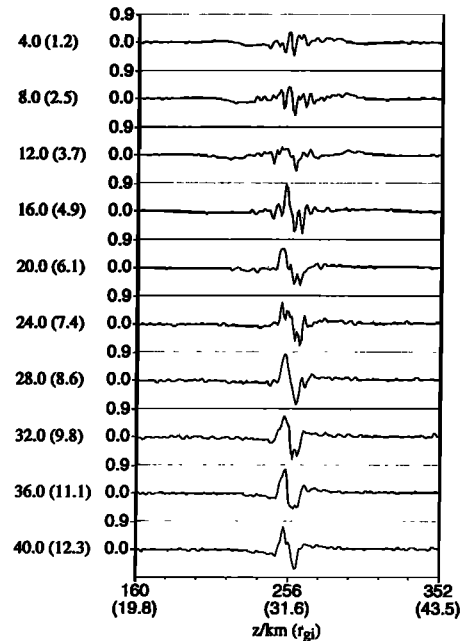

Figure 5. Evolution of the electric field component parallel to the magnetic field line $E_{\parallel}$, in units of $V m^{-1} \times 10^{-3}$. The linking field is $2nT$. The numbers down the left- hand side of each figure indicate real time in seconds (ion gyroperiods). Only the central portion of the simulation axis is shown.

bulk $V_{\parallel}$ of the trapped population increases to approximately twice $V_{A,x}$, the Alfvén speed in x. An increase in $P_{\parallel}$ accompanies the increase in $V_{\parallel}$. Once $P_{\parallel}$ has become sufficiently large to strongly perturb the bulk plasma configuration, the trapped population of ions escapes, that is, they leave the field reversal region. The escaping ions distort the magnetic field.

After the initial escape a continual process of ions becoming trapped in the well, accelerating and escaping from the well is set up. In the strong linking field case this process has a "bursty" nature, with bunching evident in the escaping ions. Also in this case, ions remain trapped in the reversal for shorter durations than with a weak linking field.

In Figure 5 we plot the component of the electric field parallel to the magnetic field direction, $E_{\parallel}$, as it evolves during the simulation (linking field $2nT$). It can be seen that $E_{\parallel}$ is nonzero in the vicinity of the field reversal and is consistent in direction with the trapping of the population within the reversal. When the initially trapped population of ions escapes from the reversal structure (at about 4.9 τ_{gi}), the region occupied by nonzero $E_{\parallel}$ contracts, and in comparison with Figure 13, it will be seen to be associated with the region within which ions are subsequently trapped rather than the distorted field region associated with the escaping ions.

4. Ion Dynamics

We will now discuss the detailed ion dynamics in both the x and z directions. Motions along z are oscillatory,

with no overall gain in velocity and possibly a net loss as the reversal expands. In the x direction there is net acceleration to approximately twice the Alfvén speed. Acceleration in x can be approximately modeled as a first-order Fermi acceleration [e.g., *Cowley*, 1980]. Motion in z is understood in terms of the electric potential ϕ (discussed in section 2.4) which has the form of a potential well.

To simplify the discussion, we first consider an ideal field reversal, where B_x changes discontinuously as a step function, treating motion in x and z as if they were decoupled. We then consider the more realistic case of a smooth reversal over a finite distance, retaining the decoupled approximation.

4.1. "Zero-order" Description

As a "zero order" approximation we suppose that at time zero, B_x reverses discontinuously from $+B_x$ to $-B_x$ (in fact, it varies smoothly on a scale larger than the resolution Δz of the simulation). The potential well in this case is a square well (Figure 6a). Evolution of the field line between two times t_0 and t_1 is illustrated in Figure 6b. As the field line relaxes, two wave structures bounding a region of zero B_x move apart in the z direction with some speed V_z. Field lines between the boundaries relax in x with a speed V_x. Our simulation results show the boundaries to have both Alfvén and slow-wave characteristics, and so V_z is determined by the Alfvén and slow wave speeds in z. By making the approximation that V_z is just the Alfvén speed along z, we now show that V_x is approximately the Alfvén speed along x.

Referring to Figure 6b, point A on the relaxing field line at time t_0 moves to point B at a later time t_1. Defining $\Delta t = t_1 - t_0$, we have $l_x = V_x \Delta t$ and $l_z = V_z \Delta t$
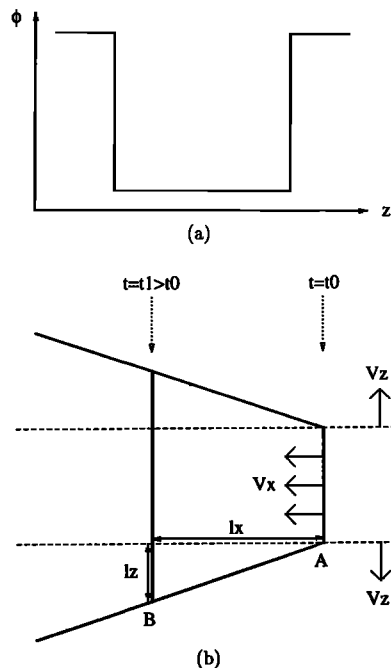

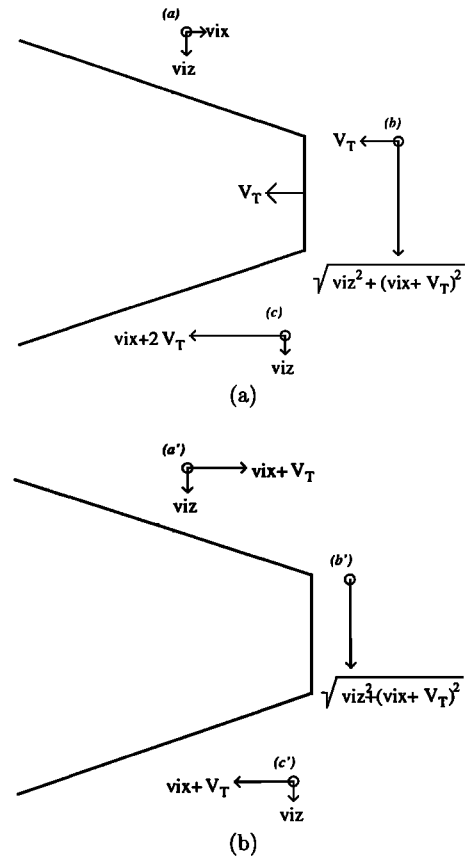**Figure 6.** (a) Potential well and (b) field line envisaged for a discontinuous reversal.

Figure 7. Frame transformation arguments for first-order Fermi acceleration. (a) Simulation rest frame. (b) Field line rest frame.

by geometry. Clearly, the line AB defines a section of field line, so $l_x/l_z = B_x/B_z$. Hence $V_x/V_z = B_x/B_z$, and if $V_z = V_{A,z}$ then $V_x = V_{A,x}$.

Given that the field line moves in $\hat{x}$ with velocity $V_T \hat{x} = V_{A,x} \hat{x}$ in the simulation rest frame, we now give a frame transformation argument leading to field-aligned ion acceleration in this frame. Refer to Figure 7. Under the decoupled assumption we ignore the expansion of the reversal, that is, motion of the field line along z. (If we include this, then the ions will lose field-aligned velocity, whilst at positions b, b' due to the expansion of the reversal). Consider an ion entering the reversal with velocity components $-v_{ix} \hat{x}$ and $-v_{iz} \hat{z}$ in the simulation rest frame (position a). We transform into the field line rest frame, where the constant convection electric field E_y is zero, by moving with velocity $V_T \hat{x}$. The ion's x velocity component becomes $-(v_{ix} + V_T) \hat{x}$ (position a'). The ion then travels across the zero-B_x region of field line (positions b, b') and exits the reversal. In the field line frame the ion's energy is constant, so its x component simply reverses, becoming $(v_{ix} + V_T) \hat{x}$ (position c'). When transformed back into the simulation rest frame this becomes $(v_{ix} + 2V_T) \hat{x}$ (position c). Thus the ion has gained twice the field line speed in the simulation rest frame, i.e., $2V_{A,x}$, in the x direction.

We should also consider the effect of the expansion of the reversal structure in z. The boundaries of the

region of zero B_x each have velocity $V_{A,z}$ along z. When an ion interacts with one of these boundaries, it will lose energy. A similar frame transformation argument to that given previously shows that the ion will lose twice the velocity of the boundary with each interaction. Hence whilst the ion approximately gains field-aligned velocity (i.e., x directed velocity) due to relaxation of the reversal in x, it will lose field-aligned velocity (z directed velocity) whilst within the reversal at positions b, b'.

4.2. "First-order" Description

We improve on the above zero-order description by considering the more realistic case where B_x reverses smoothly over a finite distance at time zero. The potential well in this case is harmonic (Figure 8a). The potential wells observed in the simulations have this form (Figures 3, 4 and 9). Evolution of the field line between two times t_0 and t_1 is sketched in Figure 8b. Two wave structures again bound the reversal region, but these are no longer confined to an infinitely thin region as in the zero-order approximation.

In this first-order model, the electric field component E_y across the reversal is not constant but varies with z (this is most pronounced in the simulations at early times). Since B_z is constant in this geometry, there is no single de Hoffman-Teller frame transformation velocity $V_T = V_x$ that would satisfy $E_y(z) = -V_x B_z = 0$, and so no single frame transformation will take us into the field line rest frame. Instead, V_T is a function of z and the above first-order Fermi acceleration arguments cannot be employed exactly. We would expect net x-directed ion acceleration to be of similar magnitude to that deduced from the zero-order model, that is, gains of less than or of order $2V_{A,x}$, but cannot predict details of the trajectories.
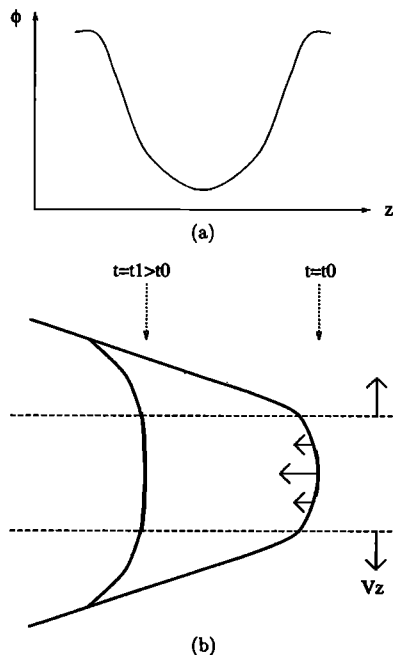

(a)

(b)

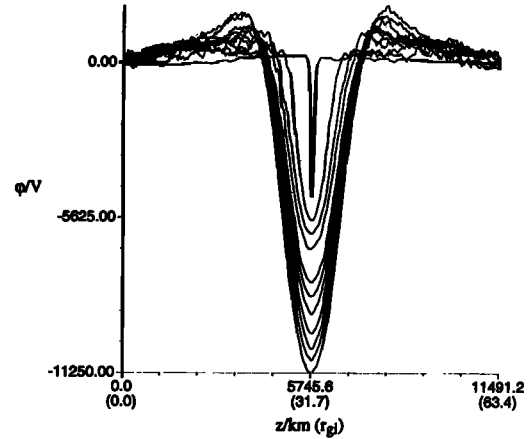**Figure 8.** (a) Potential well and (b) field line envisaged for a gradual reversal.

Figure 9. Evolution of the potential well in the case $B_z = 2nT$. The well widens and deepens in time.

The potential well in this model is harmonic, and as the field line relaxes, the potential well expands. As an ion moves into the reversal, it interacts with the expanding well and loses energy ε at a rate given by

$$\frac{d\varepsilon}{dt} = \frac{d\phi}{dt}\Big|_{trajectory\ of\ ion}. \tag{14}$$

For suitably small initial velocities v_{iz}, this loss of energy will be sufficient to render the ion in a bound state. Thus the ion becomes trapped in the reversal structure and oscillates across it. Under the approximation that motion in the x and z directions are decoupled, the trapped ion obeys the equation of motion

$$\frac{d^2z}{dt^2} = \frac{E_z q}{m}, \tag{15}$$

where $E_z = -\partial\phi/\partial z$. Such an equation of motion can be solved by taking a suitable model for the potential ϕ. A relatively simple model consists of a simple harmonic potential well of constant depth ϕ_0 expanding from an initial half width A_0 with constant velocity v; that is,

$$\phi(z,t) = \phi_0 \left[\frac{z^2}{(A_0 + vt)^2} - 1\right]. \tag{16}$$

This potential arises from a B_x which reverses linearly with z; in the simulation, $B_x \sim \tanh(z/A_0)$, so this potential results when $z << A_0$. In practice, the depth of the potential well is observed to increase with time as the field relaxes (Figure 9); this is not included in the simple model. The equation of motion using equation (16) for ϕ is solved in the appendix. It is interesting to consider the motion of a population of trapped ions, as described by v_z versus z phase space plots. The analysis given in the appendix predicts that these plots should have a marked spiral appearance (Figure 10a). This is borne out by simulation results for times prior to excessive phase mixing, after which the spiral appearance is obscured by thermal effects (Figure 10b).
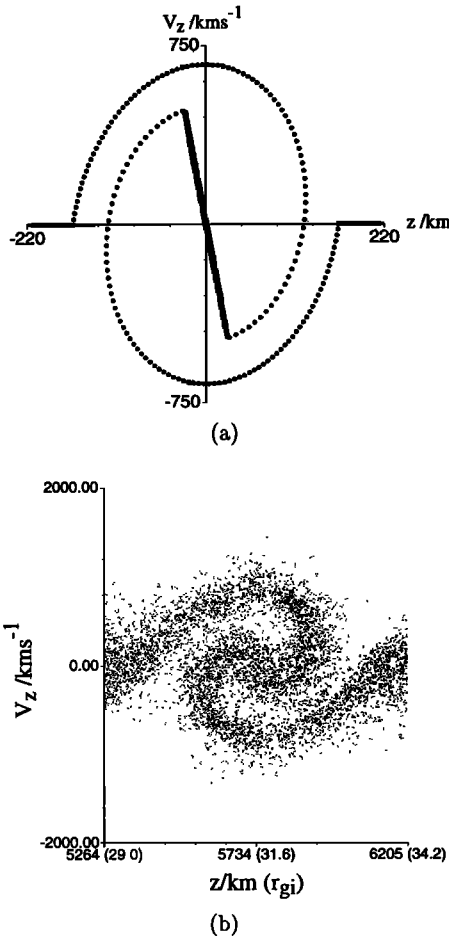
(a)

(b)

Figure 10. phase space plots of v_z versus z as (a) deduced by solving the equations of motion of many particles placed initially uniformly across an an expanding harmonic potential well of constant depth (b) observed in simulation results.

4.3. Effect of Linking Field Strength

Typical ion v_x versus z trajectories are given in Figure 11 for both simulations. In both cases the ion starts with a small thermal v_x, and as it oscillates back and forth across the reversal, it gains in v_x. The maximum net field aligned velocity an individual ion can gain before it escapes from the potential well is $\sim 2V_{A,x}$ as shown in sections 4.1 and 4.2. In the weak linking field case the ion's net v_x jumps by small fractions of $V_{A,x}$ over each oscillation, whilst with a strong linking field the ion's net v_x increases much more quickly. As we would expect, ions which have the least number of interactions with the walls of the expanding potential well before escaping from it will ultimately have greater net field-aligned velocity. We will show that the bulk parallel pressure of the trapped population dictates when the trapped ions will initially escape, rather than the velocity of individual ions.

After performing a number of oscillations in the potential well, trapped ions escape from the well and travel away from the reversal to either end of the simulation box. This is illustrated in Figure 12, which shows the

z versus t trajectories of several ions. The two plots for the weak linking field case reveal that ions remain trapped for longer periods than with a strong linking field. It is also evident that after the escape of the initially trapped population started where $B_x \ll B_z$, ions which were originally located outside the reversal where $B_x \gg B_z$ continue to fall into the well, accelerate, and escape.

It is significant that the initial escape happens en masse for the trapped population, indicating a bulk plasma mechanism rather than a process solely dictated by single particle dynamics.

5. Bulk Fluid Behavior

Taking the pressure tensor for ions in the vicinity of the field reversal to be gyrotropic, we calculate $P_\parallel$ and $P_\perp$ for the trapped population [*Krall and Trivelpiece*, 1986] (this assumption has been found to be good to within 10%). We find that as the ions gain field-aligned velocity, $P_\parallel$ increases on the timescale of trapped ion oscillation. When the difference between $P_\parallel$ and $P_\perp$ is sufficiently large, the quasi-static equilibrium of the trapping phase breaks down (Figure 13). The trapped population escapes from the reversal region, traveling toward either boundary of the simulation box. As they do so, they distort the magnetic field and bulk plasma properties.
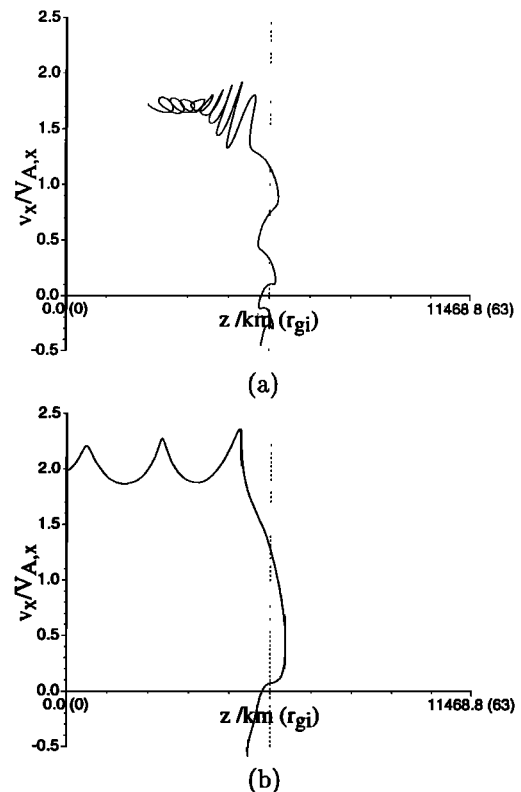

(a)

(b)

Figure 11. Typical z versus v_x ion trajectories in the simulation frame for (a) $B_z = 2nT$ and (b) $B_z = 8nT$. The dashed line indicates the center of the reversal. After exiting the reversal, the ions (moving to the left here) execute gyromotion.
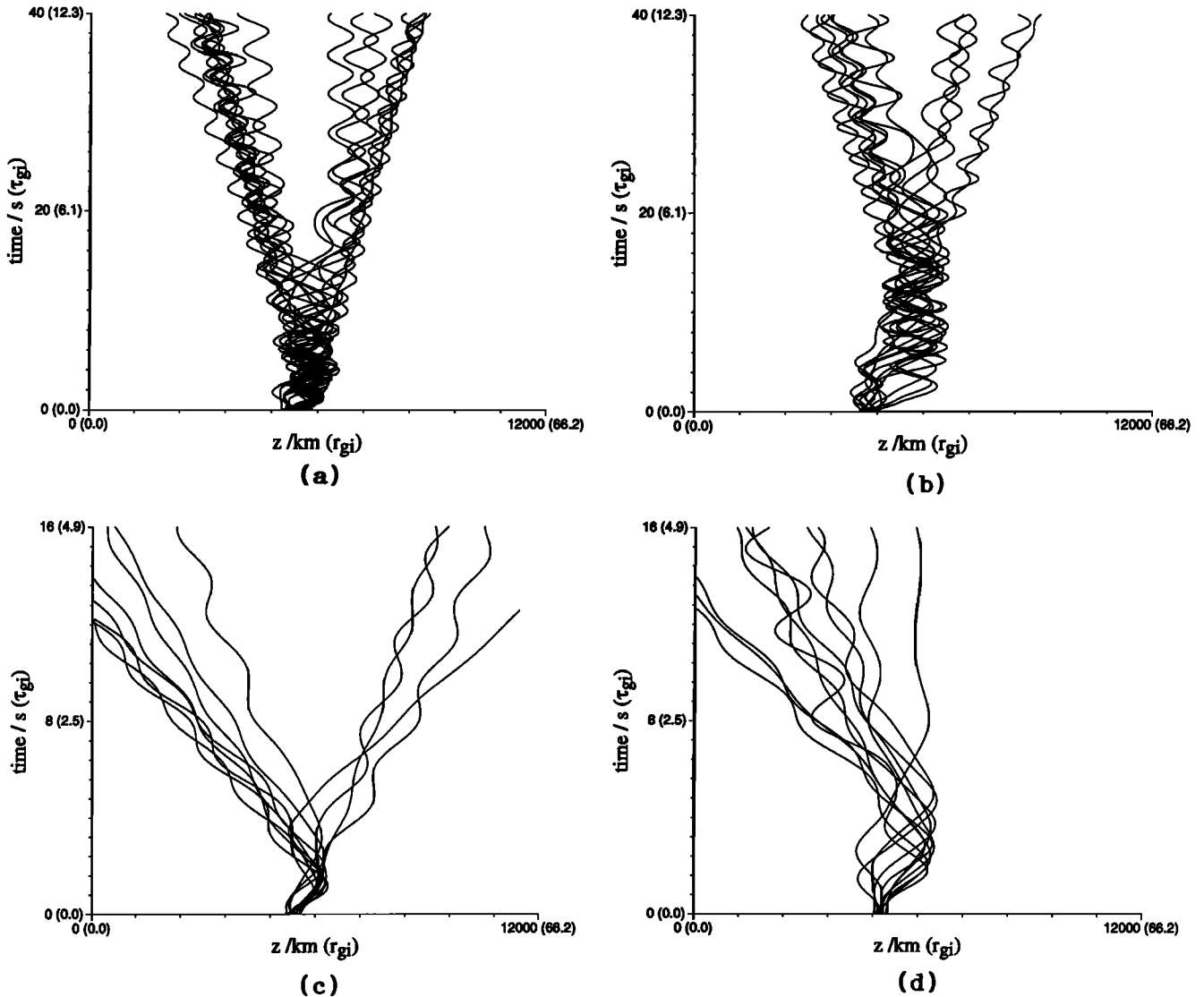
Figure 12. The trajectories of several ions initiated (a) and (c) close to the reversal (b) and (d) some way from the reversal. The top two figures (a,b) are for $B_z = 2nT$, the bottom two (c,d) for $B_z = 8nT$.

The increase in $P_\parallel$ is consistent with the combined effects of Fermi acceleration and the trapping force discussed earlier. These result in an increased spread in the parallel velocities of the trapped ions. This can be seen in Figure 14, which gives shaded $v_\parallel$ versus z phase space plots.

As we see in Figure 13 (and Figures 3 and 4), the trapped population initially escapes en masse from the reversal region when locally $P_\parallel$ is sufficiently large that

$$P_\parallel - P_\perp \simeq \frac{B^2}{2\mu_0} \qquad (17)$$

This condition is just that which double adiabatic theory would indicate as when the excess $P_\parallel$ will force a reconfiguration in the bulk plasma properties [*Krall and Trivelpiece*, 1986]. When this happens, the quasi-static trapping phase breaks down and the trapped ions es-

cape from the reversal region. The anisotropy of $P_\parallel$ and $P_\perp$ has been discussed by other authors [e.g., *Pritchett and Coroniti*, 1992] as an equilibrium condition arising from double adiabatic theory [e.g., *Bittencourt*, 1986]. Here however, it appears in a dynamic context as an indicator of particle escape from the reversal.

Figure 13 shows that in the weak linking field case the trapped ions achieve pressure balance at initial escape, that is, $P_\parallel - P_\perp \simeq B^2/2\mu_0$, whilst in the strong linking field case the trapped population produce an overpressure, $P_\parallel - P_\perp > B^2/2\mu_0$. In the former case, individual ion $v_\parallel$ values increase in small jumps as they oscillate across the reversal and the bulk $P_\parallel$ can approach the escape condition gradually. In the latter case, individual ion $v_\parallel$ values jump by much larger amounts during oscillation across the reversal, and consequently, $P_\parallel$ exceeds the escape requirement.

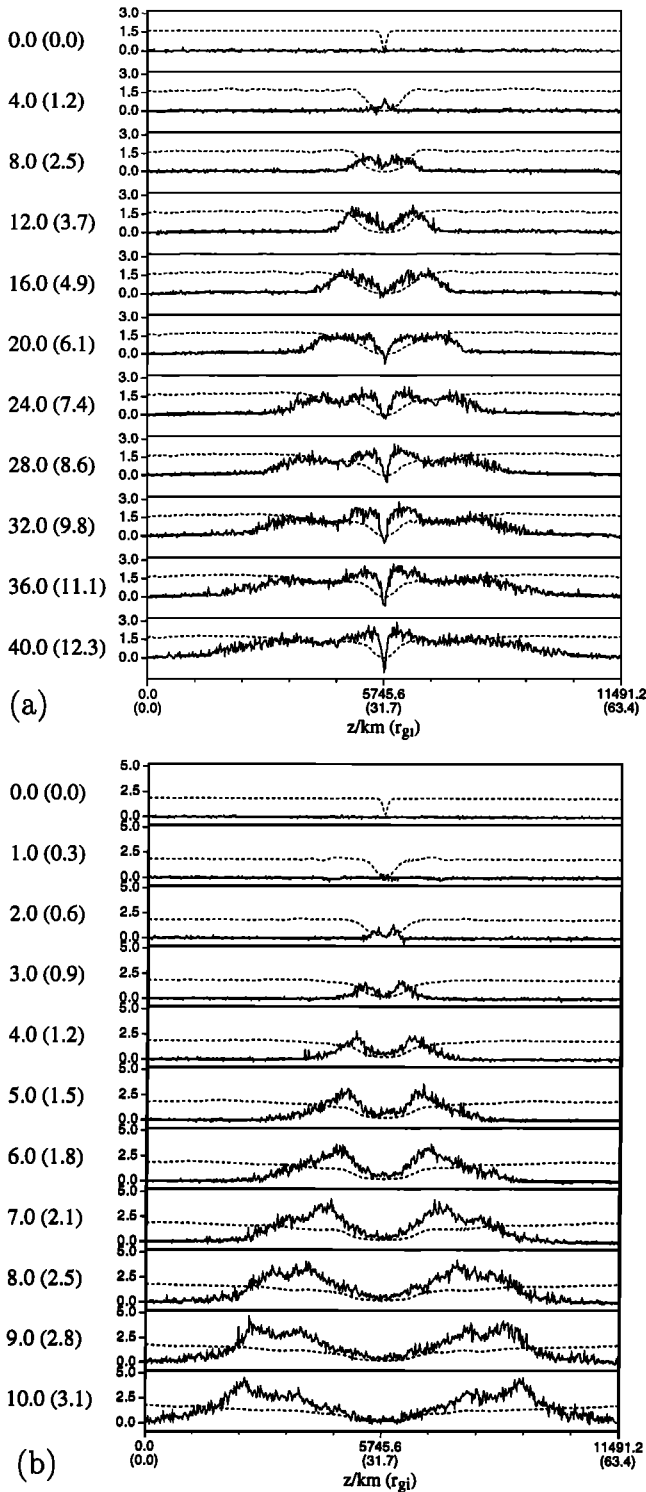The applicability of equation (17) can be tested by rearranging it to give

Figure 13. Evolution of $P_\| - P_\perp$ (solid line) and magnetic field pressure P_B (dashed line) with (a) a weak linking field (b) a strong linking field. The units of pressure are $Nm^{-2} \times 10^{-10}$. The numbers down the left-hand side of each figure indicate real time in seconds (ion gyroperiods).

$$P_\| \simeq P_\perp + \frac{B^2}{2\mu_0}. \tag{18}$$

Calculating the right-hand side from simulation plasma parameters would yield the value of $P_\|$ required to sat-

isfy (17) locally. This $P_\|$ can then be related to the bulk $v_\|$ of the plasma by assuming a form for the distribution function of the ions. For simplicity, we assume that the trapped populations are just two beams with bulk parallel velocities $\pm v_{crit}$, as shown in Figure 15. In this case, $P_\|$ is given by

$$P_\| = \rho v_{crit}^2. \tag{19}$$

Thus

$$v_{crit} = \sqrt{\frac{P_B + P_\perp}{\rho}} \tag{20}$$

where P_B is the magnetic field pressure $B^2/(2\mu_0)$.

Using the simulation bulk parameters, $\pm v_{crit}$ has been plotted on the phase space plots of Figure 14. In the pre-escape plots of both simulations, although some trapped ions have individual parallel velocities greater than the boundary v_{crit} escape does not occur as the bulk parallel velocity is less than this v_{crit}. In the post escape plots it is clear that the bulk parallel velocity of the escaping population is greater than v_{crit}, thus satisfying the escape criterion.

The post escape plot for the strong linking field case in Figure 14 also shows clearly the bunching of the escaping ions. This does not arise in the weak linking field case.

5.1. Magnetic Fields

Although B_y is zero in our initial conditions, a characteristic bipolar B_y signature is generated across the reversal from early times (see Figures 3 and 4). Hodograms of the B_x, B_y field components are given in Figure 16 (see also [Goodrich and Cargill, 1991]). As we move through the structure with increasing z, the field rotates in a clockwise (right-handed) sense through an angle less than $\pi/2$, and then back again in an anticlockwise (left-handed) sense. In the regions at the edges of the reversal, where B_y increases from zero, the total field strength B is constant and the density reduces.

To support B_y, the electrons carry current in the $-\hat{x}$ direction and the ions in $+\hat{x}$. In both simulations, the electron current is approximately 25% larger than the ion current, and so there is a net current in $-\hat{x}$. Prior to escape from the reversal, the electron current reverses direction at the edges of the reversal to thus support the fine structure. After escape the field becomes distorted, and fine structure is not as evident.

When the linking field is weak, the magnitude of B_y is approximately twice that observed when the linking field is strong. This may be due to the much longer time for which ions are trapped in the reversal structure in the former case, giving the B_y component more time to develop.

The post escape hodograms, Figures 16b and 16d, show more structure in the strong linking field case than in the weak case. This corresponds to fluctuations in B_x and B_y at locations of particle bunching in the escaping ions.
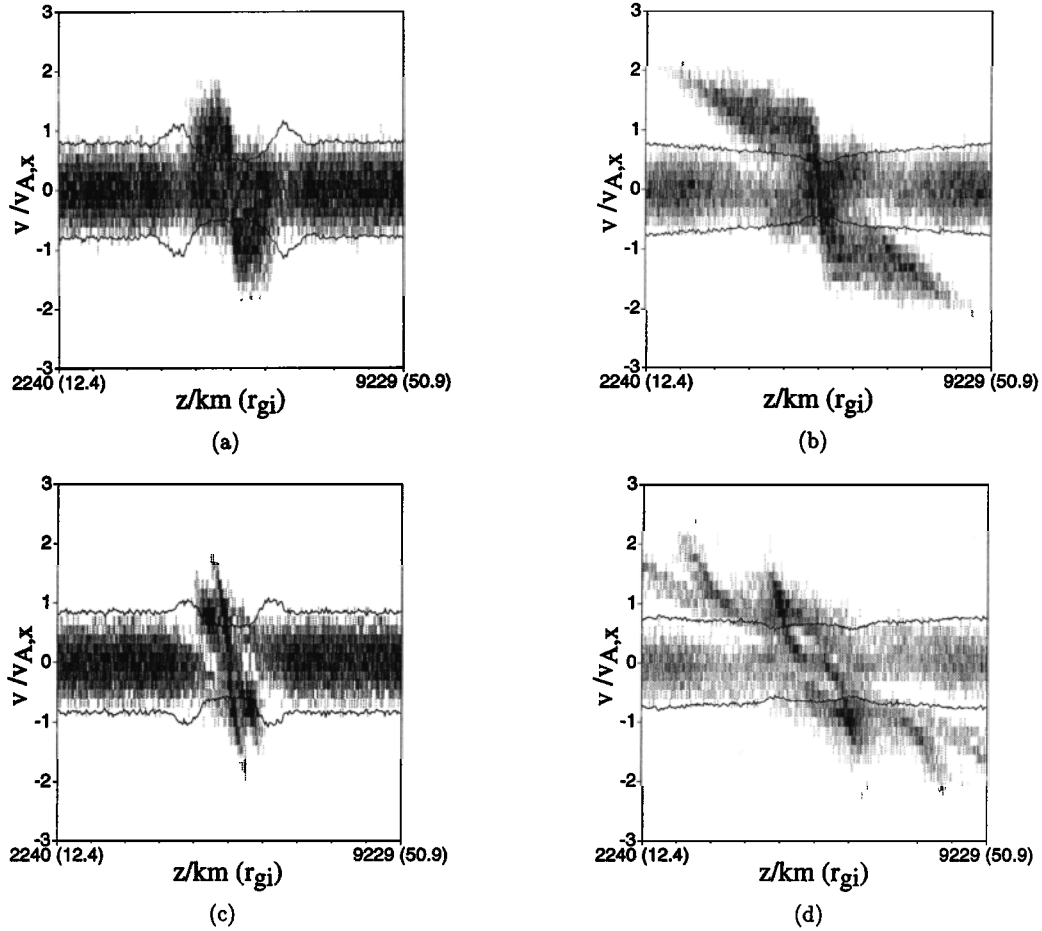
(a)

(b)

(c)

(d)

Figure 14. Shaded $v_\parallel$ versus z phase space plots. The top two figures (a,b) are for a weak linking field $(2nT)$, the bottom two (c,d) for a stronger linking field $(8nT)$. In each case the leftmost plot (a,c) is for a time prior to escape, the rightmost plot (b,d) is post escape (the plots are for the same times as the snapshots in Figures 3 and 4). Note that only the central 60% of the simulation axis is shown, to clarify structure in the escaping population. The increased spread in parallel velocities in the reversal structure can clearly be seen in both pre-escape plots. In the weak linking field case, the ions escape from the reversal with velocities less than twice the x direction Alfvén speed. With a stronger linking field, they escape with twice the Alfvén speed. The solid lines indicate the critical velocity deduced from $P_\parallel - P_\perp = B^2/2\mu_0$. In both simulations, escape from the reversal only occurs when the bulk parallel velocity of the trapped ions exceeds this critical velocity.

6. Conclusions

We have presented the results of one-dimensional, self-consistent simulations of a dipolarizing field reversal with varying linking field strengths. We have discussed both ion dynamics and bulk plasma behavior. Our principal results are as follows:

1. The large ∇B^2 in the reversal structure causes the trapping of inflowing ions.

2. The $P_\parallel$ of the trapped population increases in a manner consistent with net field aligned acceleration due to the Fermi acceleration of ions as they oscillate across the reversal and deceleration as they interact with the reversal edge. This ultimately results in their escape.

3. We have found a general condition,

$$P_\parallel - P_\perp \gtrsim \frac{B^2}{2\mu_0} \qquad (21)$$

which describes when the trapped plasma can no longer be contained and will escape.

4. Following this initial escape a continual process of inflowing ions becoming trapped in the reversal, accelerating and subsequently escaping occurs.
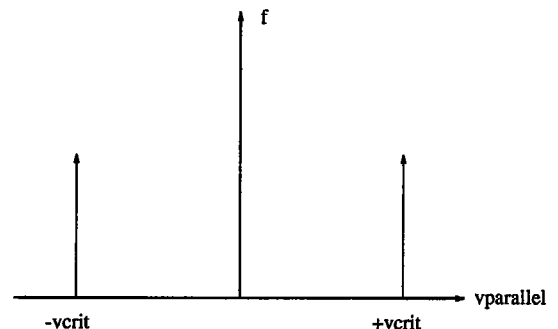

Figure 15. Distribution function assumed for calculating v_{crit}, $f(v_\parallel) = f_0(\delta(v_\parallel - v_{crit}) + \delta(v_\parallel + v_{crit}))$
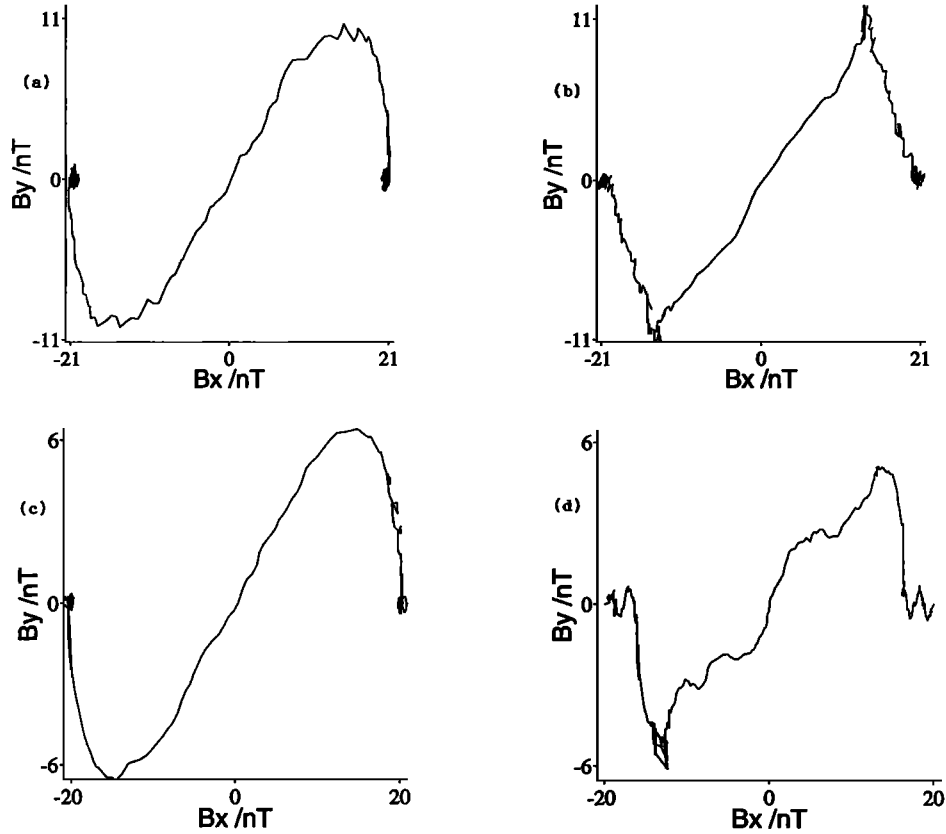
Figure 16. Hodograms showing the bipolar B_y component which is generated from early times. The top two graphs (a,b) are for a weak ($2nT$) linking field, the lower two (c,d) for a stronger linking field ($8nT$). In each case, the left figure (a,c) is prior to escape of the trapped ions and the figure on the right (b,d) is post escape.

5. We have identified a characteristic signature in B_y accompanying this behavior.

6. We have shown that the time an ion remains trapped is dictated by the ratio of linking field component to reversing component, and as a consequence, this determines whether the post escape phase is characterized by pressure balance ($P_\parallel - P_\perp \simeq P_B$) or overpressure ($P_\parallel - P_\perp > P_B$).

These results define a signature which should be evident in observations of dipolarization close to the tail center plane. If $P_\parallel - P_\perp \geq P_B$ outside of the reversal, then field aligned beams moving at $V_\parallel \sim 2V_{A,x}$ ($\sim 1 - 10keV$ from the simulation results shown here) will be observed which, if $P_\parallel - P_\perp \gg P_B$, will be bursty in nature. Inside the weak field region (identifiable by the bipolar B_y signature in a coordinate system analogous to the simulation configuration) counterstreaming beams of $V_\parallel < 2V_{A,x}$ should be observable.

Our simulations reveal a local ion energization mechanism which can be approximately modeled as first-order Fermi acceleration. Ions are accelerated to low-medium energies ($1 - 10keV$), indicating that the high-energy ($\sim 1MeV$) bursts of particles seen during substorms must be accelerated elsewhere or by some other mechanism not represented in the self-consistent hybrid code.

Appendix: Expanding Potential Well

To represent an expanding potential well of constant depth in one dimension, we consider a potential of the form

$$\phi(z,t) = \phi_0 \left[\frac{z^2}{(A_0 + vt)^2} - 1 \right], \tag{A1}$$

where A_0 is the initial half width and v is the speed at which the edges of the well move apart. The electric field associated with this potential is given by

$$
\begin{aligned}
E(z,t) &= -\frac{\partial \phi}{\partial z} \\
&= -\frac{2\phi_0 z}{(A_0 + vt)^2}
\end{aligned}
\tag{A2}
$$

A particle of mass m and charge q in this potential has the equation of motion

$$\frac{d^2 z}{dt^2} + \left(\frac{2\phi_0 q}{mA_0^2} \right) \frac{z}{(1 + vt/A_0)^2} = 0. \tag{A3}$$

To solve this, we make two substitutions. First, we substitute $T = 1 + vt/A_0$ and obtain

$$\left(\frac{v}{A_0}\right)^2 \frac{d^2z}{dT^2} + \left(\frac{2\phi_0 q}{mA_0^2}\right)\frac{z}{T^2} = 0 \qquad (A4)$$

or

$$\frac{d^2z}{dT^2} + k\frac{z}{T^2} = 0 \qquad (A5)$$

where k is the dimensionless constant $(2\phi_0 q/mv^2)$. We now make a second substitution, $T = e^s$ yielding

$$\frac{d^2z}{ds^2} - \frac{dz}{ds} + kz = 0 \qquad (A6)$$

Equations of this form are associated with damped simple harmonic motion. To solve it we consider the auxiliary equation,

$$D^2 - D + k = 0 \qquad (A7)$$

which has roots

$$D = \frac{1}{2} \pm \sqrt{\frac{1}{4} - k}. \qquad (A8)$$

The case $k < 1/4$ would correspond to overdamped motion. This is outside the regime of our simulations, where we have $k > 1/4$. The standard solution in this case is

$$z = Ce^{\frac{s}{2}} \sin[s\sqrt{k - \tfrac{1}{4}} + \gamma] \qquad (A9)$$

where C and γ are constants determined by the boundary conditions. Substituting back for s and T gives

$$z = C\sqrt{\left(1 + \frac{vt}{A_0}\right)} \sin[\sqrt{(k - \tfrac{1}{4})}\ln(1 + \frac{vt}{A_0}) + \gamma] \quad (A10)$$

From this we see that the amplitude of oscillation increases with time as $\sqrt{(1 + vt/A_0)}$. The period of the motion also increases due to the logarithmic dependence on t in the oscillatory term (Figure 17).

The boundary conditions, and hence the constants C and γ, are dependent upon whether the particle's initial position z_0 lies inside or outside the potential well at time $t = 0$. For the two cases we have

$$\text{If } z_0 < A_0, \quad z = z_0, \frac{dz}{dt} = 0 \quad t = 0 \qquad (A11)$$
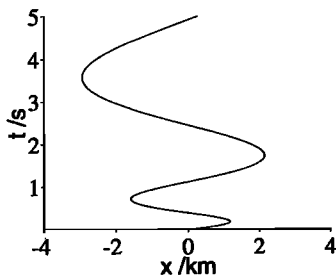
Figure 17. A typical trajectory obtained by solving the equation of motion of a particle in an expanding harmonic potential well of constant depth.

$$\text{If } z_0 > A_0, \quad z = z_0, \frac{dz}{dt} = 0 \quad t \le \frac{z_0 - A_0}{v} \quad (A12)$$

Using these boundary conditions, we can obtain expressions for C and γ, giving if $z_0 < A_0$

$$\gamma = \tan^{-1}[-2\sqrt{k - \tfrac{1}{4}}] \qquad (A13)$$

$$C = \frac{z_0}{\sin[\gamma]} \qquad (A14)$$

and if $z_0 > A_0$

$$\gamma = \tan^{-1}[-2\sqrt{k - \tfrac{1}{4}}] - \sqrt{k - \tfrac{1}{4}}\ln(\tfrac{z_0}{A_0}) \quad (A15)$$

$$C = \frac{\sqrt{z_0 A_0}}{\sin[\sqrt{k - \tfrac{1}{4}}\ln(\tfrac{z_0}{A_0}) + \gamma]} \qquad (A16)$$

If we now populate the vicinity of the potential well with a number of equally spaced particles, we can obtain the expected phase space diagram. This involves calculating both the position and the velocity of each particle at a given time; the latter quantity is given by

$$v_z = \frac{dz}{dt}$$
$$= \frac{vC}{A_0\sqrt{(1 + \frac{vt}{A_0})}}\{\tfrac{1}{2}\sin[\sqrt{k - \tfrac{1}{4}}\ln(1 + \frac{vt}{A_0}) + \gamma]$$
$$+ \sqrt{k - \tfrac{1}{4}}\cos[\sqrt{k - \tfrac{1}{4}}\ln(1 + \frac{vt}{A_0}) + \gamma]\} \quad (A17)$$

A typical phase space plot obtained by this method is given in Figure 10a, to be compared with an actual plot obtained from a simulation given in Figure 10b.

As a final test of this solution, taking the limit of $v \to 0$ should give us the trajectory of a particle in a potential well of fixed width. To do this, we note that as $v \to 0$,

$$\ln(1 + \frac{vt}{A_0}) \to \frac{vt}{A_0}, \qquad (A18)$$

and with some manipulation, equation (A10) becomes

$$z = C\sin[\sqrt{\left(\frac{2\phi_0 q}{mA_0^2}\right)}t + \gamma] \qquad (A19)$$

Comparing this with the equation of SHM,

$$z = C\sin[\omega t + \gamma] \qquad (A20)$$

we identify

$$\omega = \sqrt{\frac{2\phi_0 q}{mA_0^2}} \qquad (A21)$$

as being the frequency of oscillation. In the case of a slowly expanding potential well, the frequency would have this value at time $t = 0$, and it would slowly decrease thereafter.

Thcussions. One of the authors (A.R.) was supported by a SERC scholarship.

The Editor thanks two referees for their assistance in evaluating this paper.

References

Ashour-Abdalla, M., J. Buchner, and L. M. Zelenyi, The quasi-adiabatic ion distribution in the central plasma sheet and its boundary layer, *J. Geophys. Res., 96*, 1601, 1991.

Baumjohann, W., G. Paschmann, and C. A. Cattell, Average plasma properties in the central plasma sheet, *J. Geophys. Res., 94*, 6597, 1989.

Bittencourt, J. A., *Fundamentals of Plasma Physics*, Pergamon, New York, 1986.

Chapman, S. C., Chaotic single particle dynamics in a multitimescale parameterizable field reversal, *Ann. Geophys., 11*, 239, 1993.

Chapman, S. C., Properties of single particle dynamics in a parabolic magnetic reversal with general time dependence, *J. Geophys. Res., 99*, 5977, 1994.

Chapman, S. C. and M. W. Dunlop, Ordering of momentum transfer along V × B in the AMPTE solar wind releases, *J. Geophys. Res., 91*, 8051, 1986.

Chapman, S. C. and S. J. Schwartz, One-dimensional hybrid simulations of boundary layer processes in the AMPTE solar wind lithium releases, *J. Geophys. Res., 92*, 11059, 1987.

Cowley, S. W. H., Plasma populations in a simple open model magnetosphere, *Space Sci. Rev., 26*, 217, 1980.

Delcourt, D. C., Mid-tail ion dynamics at substorm onset, in *Magnetic Substorms*, Geophysical Monogr. Ser. vol. 64, AGU, Washington, D. C., 1991.

Delcourt, D. C., and T. E. Moore, Precipitation of ions induced by magnetotail collapse, *J. Geophys. Res., 97*, 6405, 1992.

Goodrich, C. C., and P. J. Cargill, An investigation of the structure of rotational discontinuities, *Geophys. Res. Lett., 18*, 65, 1991.

de Hoffman, F., and E. Teller, Magneto- Hydrodynamic shocks, *Phys. Rev., 80*, 692, 1950.

Hones Jr, E. W., I. D. Palmer, and P. R. Higbie, Energetic protons of magnetospheric origin in the plasma sheet associated with substorms, *J. Geophys. Res., 81*, 3866, 1976.

Krall, N. A., and A. W. Trivelpiece, *Principles of Plasma Physics*, San Francisco Press. Inc., San Francisco, Calif., 1986.

Lennartsson, W., R. D. Sharp, E. G. Shelley, R. G. Johnson, and H. Balsiger, Ion composition and energy distribution during 10 magnetic storms, *J. Geophys. Res., 86*, 4628, 1981.

Leroy, M. M., Structure of perpendicular shocks in collisionless plasma, *Phys. Fluids, 26*, 2742, 1983.

Pritchett, P. L. and F. V. Coroniti, Formation and stability of the self-consistent one-dimensional tail current sheet, *J. Geophys. Res., 97*, 16773, 1992.

Swift, D. W., Effects of ion demagnetization in the plasma sheet, *J. Geophys. Res., 97*, 16803, 1992.

Swift, D.W. and C. Allen, Interaction of the plasma sheet with the lobes of the Earth's magnetotail, *J. Geophys. Res., 92*, 10015, 1987.

Terasawa, T., M. Hoshino, J.-I. Sakai and T. Hada, Decay instability of finite-amplitude circularly polarized Alfvén waves: A numerical study of stimulated Brillouin scattering, *J. Geophys. Res., 91*, 4171, 1986.

Thomas, V. A., D. Winske and N. Omidi, Re-forming supercritical quasi-parallel shocks 1. One- and two-dimensional simulations, *J. Geophys. Res., 95*, 18809, 1990.

Wagner, J. S., J. R. Kan and S.-I. Akasofu, Particle dynamics in the plasma sheet, *J. Geophys. Res., 84*, 891, 1979.

S. C. Chapman, Space Science Centre(MAPS), University of Sussex, Falmer, Brighton BN1 9QH, United Kingdom. S.C.Chapman@uk.ac.sussex

A. Richardson, Tessella Support Services, Abingdon, OX14 3PX, United Kingdom. rica@uk.co.tessella